

# Planetesimal formation via the streaming instability persists under turbulence driven by magnetorotational instability

Linn E. J. Eriksson<sup>1</sup>, Ziyang Xu<sup>2</sup>, Jeonghoon Lim (임정훈)<sup>3</sup>, Chao-Chin Yang (楊朝欽)<sup>4</sup>, Pinghui Huang<sup>5</sup>, and Mordecai-Mark Mac Low<sup>1</sup>

<sup>1</sup> Department of Astrophysics, American Museum of Natural History, 200 Central Park West, New York, NY 10024, USA  
e-mail: leriksson@amnh.org

<sup>2</sup> Center for Star and Planet Formation, GLOBE Institute, University of Copenhagen, Øster Voldgade 5–7, 1350 Copenhagen, Denmark

<sup>3</sup> Department of Physics and Astronomy, Iowa State University, Ames, IA 50010, USA

<sup>4</sup> Department of Physics and Astronomy, The University of Alabama, PO Box 870324, Tuscaloosa, AL 35487-0324, USA

<sup>5</sup> CAS Key Laboratory of Planetary Sciences, Purple Mountain Observatory, Chinese Academy of Sciences, Nanjing 210023, People's Republic of China

Received Month day, year

## ABSTRACT

Clumping by streaming instability (SI) leading to gravitational collapse is the leading proposed mechanism for forming planetesimals, the building blocks of terrestrial planets and giant-planet cores. The critical dust-to-gas density ratio above which the SI leads to dust concentration strong enough to result in collapse depends on local dust properties and disk conditions, such as particle Stokes number, pressure gradient, and turbulence. The role of turbulence has recently drawn attention because simulations have shown that even modest levels of isotropically forced turbulence can significantly increase the critical dust-to-gas ratio. However, we show that this does not hold for turbulence self-consistently generated by the magnetorotational instability (MRI). We present the first parameter study of the SI in three-dimensional, stratified, shearing-box simulations including non-ideal magnetohydrodynamics with ambipolar diffusion. Modest turbulence yields a clumping boundary similar to pure SI cases, while stronger turbulence does increase the critical dust-to-gas density ratio, though less than in the models where turbulence is isotropically forced. Particle concentration occurs inside zonal flows, large-scale structures generated by the MRI. Our results suggest that self-consistent, MRI-driven turbulence does not necessarily inhibit planetesimal formation.

**Key words.** Planets and satellites: formation – Turbulence – Magnetohydrodynamics

## 1. Introduction

The first step in the planet formation process is the collisional coagulation of micron-sized dust grains into roughly millimeter-sized pebbles. Continued growth toward planetesimal sizes is hindered by multiple growth barriers, most notably the fragmentation barrier (e.g. Blum & Wurm 2008; Güttler et al. 2010) and the radial drift barrier (e.g. Weidenschilling 1977; Birnstiel et al. 2012). Highly porous dust aggregates have been proposed as a possible way to circumvent these barriers, but this remains controversial (see discussion in Drażkowska et al. 2023). More attention has been paid to planetesimal formation via the direct gravitational collapse of dense pebble clumps. Multiple mechanisms can concentrate solids to planetesimal-forming densities, but currently the most promising one is the streaming instability (SI; Youdin & Goodman 2005; Johansen & Youdin 2007a). The SI arises from the exchange of angular momentum between gas and solid particles via aerodynamic coupling and leads to the formation of radially narrow particle filaments (Yang & Johansen 2014; Li et al. 2018) that can reach densities high enough for gravitational collapse (Johansen et al. 2015; Simon et al. 2016). SI simulations have successfully produced planetesimal populations consistent with properties of Solar System minor bodies, including the size distribution of the asteroids (Johansen et al. 2015) and cold classical Kuiper

Belt objects (KBOs) (Kavelaars et al. 2021), the orbital properties of trans-Neptunian binaries (Nesvorný et al. 2019), and the shapes (Barnes et al. 2025) and prevalence of contact binaries (Barnes et al. 2026) among the cold classical KBOs.

Identifying the conditions under which the SI leads to planetesimal formation is an active area of research. The growth rate of the linear, unstratified SI depends mainly on the particle-to-gas volume density ratio  $\epsilon$  and the Stokes number

$$St \equiv t_{\text{stop}} \Omega_K, \quad (1)$$

also referred to as the dimensionless stopping time, where the stopping time  $t_{\text{stop}}$  is proportional to the particle size and  $\Omega_K$  is the Keplerian orbital frequency (Youdin & Goodman 2005). Early studies of the SI showed that both the linear growth rate and nonlinear clumping are stronger when  $\epsilon \gtrsim 1$  (Youdin & Goodman 2005; Johansen & Youdin 2007b). In the nonlinear regime, the clumping criterion for the monodisperse SI has been extensively investigated using 2D axisymmetric, vertically stratified simulations (Carrera et al. 2015; Yang et al. 2017; Li & Youdin 2021; Lim et al. 2025b). These studies have quantified the boundary above which clumping occurs in terms of  $St$ , together with  $\epsilon$ , the particle-to-gas surface density ratio  $Z$ , or both. In addition, the clumping boundary depends on the radial pressure gradient, with lower pressure gradients allowing clump formation at lower particle-to-gas densities for a given  $St$

Table 1: Fitting parameters for the SI boundary by L25 (eq. 2) and L24 (eq. 3).

No turb. (L25)	$A$	$B$	$C$	
	0.51	0.65	-2.56	
Forced turb. (L24)	$A'$	$B'$	$C'$	$D'$
$\alpha_D$	0.15	-0.24	-1.48	1.18
$\alpha_z$	0.13	-0.28	-1.74	1.09

(Bai & Stone 2010c; Sekiya & Onishi 2018). The most recent of these studies, Lim et al. (2025b), found that the clumping boundary lies at subsolar metallicities for  $St \gtrsim 0.01$ .

Extending these results to three dimensions (3D), Lim et al. (2025a, hereafter L25), performed a parameter study of the monodisperse SI. The transition from 2D to 3D simulations results in further reduced (subsolar)  $Z_{\text{crit}}$  for  $St \gtrsim 0.03$ , increased and supersolar  $Z_{\text{crit}}$  for  $St \leq 0.02$ , and a sharp transition between these two values of  $St$ . They derived the following fit to the strong-clumping boundary:

$$\log Z_{\text{crit}}(St) = A(\log St)^2 + B \log St + C \quad \text{for } St > 0.025, \quad (2)$$

where the fitting parameters are given in Table 1 and  $Z_{\text{crit}}$  is the critical dust-to-gas surface density ratio above which the maximum particle density exceeds the Hill density.

All these criteria were derived in the absence of external turbulence; however, observations suggest that disks are at least weakly turbulent (e.g. Villenave et al. 2022; Pinte et al. 2023). Lim et al. (2024, hereafter L24) performed a parameter study of the monodisperse SI under externally driven (forced) turbulence using 3D stratified simulations that include self-gravity of particles. They obtained the following fit to the clumping boundary for gravitational collapse:

$$\log Z_{\text{crit}}(St, \alpha_{z,D}) = A'(\log \alpha_{z,D})^2 + B' \log St \log \alpha_{z,D} + C' \log St + D' \log \alpha_{z,D}, \quad (3)$$

where the fitting parameters are given in Table 1. The fit is tested over the range  $\alpha_D \in [10^{-4}, 10^{-3}]$  and  $St \in [10^{-2}, 10^{-1}]$ . The original fit was presented only in terms of the turbulent parameter for the spatial diffusion of turbulent gas,  $\alpha_D$ . Here we also express the fit in terms of the turbulent parameter for vertical diffusion,  $\alpha_z$ .

A comparison between the fits from L24 and L25 shows that forced turbulence significantly weakens SI-driven clumping, yielding supersolar  $Z_{\text{crit}}$  even in the case of relatively weak turbulence ( $\alpha_D = 10^{-4}$ ). However, the turbulence used in the simulations of L24 is isotropic and uncorrelated in time, unlike turbulence driven by several (magneto)hydrodynamical processes that can operate in protoplanetary disks, such as the vertical shear instability (VSI; Nelson et al. 2013) and the magnetorotational instability (MRI; Velikhov 1959; Chandrasekhar 1960; Balbus & Hawley 1991). In this work, we focus on MRI-driven turbulence, while referring to treatments of SI in VSI by Schäfer & Johansen (2022) and Schäfer et al. (2025).

In the regime of ideal magnetohydrodynamics (MHD), where the gas is sufficiently ionized and well coupled to the magnetic field, the MRI drives strong turbulence that efficiently redistributes angular momentum and facilitates disk accretion. For the most part, however, protoplanetary disks are expected to be weakly ionized, leading to three nonideal MHD effects – ohmic resistivity, the Hall effect, and ambipolar diffusion (AD) – which dominate different regions of the disk. Ohmic resistivity and AD

are both dissipative and act to stabilize the MRI. In the mid-plane of the disk where the SI occurs, Ohmic resistivity dampens turbulence in the inner disk, and AD dampens turbulence in the outer disk (Bai & Stone 2011). Strong clumping has been observed in simulations with ideal MHD (Johansen et al. 2007, 2011), Ohmic resistivity (Yang et al. 2018), and AD (Xu & Bai 2022; Huang & Bai 2025a). Our study focuses on planetesimal formation in the outer disk, where AD is the dominant nonideal MHD effect and MRI is the primary driver of turbulence. (The SI itself also drives turbulence, but only weakly.)

Xu & Bai (2022) found that the inclusion of modest turbulence driven by the MRI with AD leads to lower  $Z_{\text{crit}}$  for clumping compared to pure SI simulations. This is due to the spontaneous formation of long-lived density and pressure variations by the MRI turbulence – so-called zonal flows (Johansen et al. 2009) – in which particles concentrate. They found that concentration inside zonal flows and dust back-reaction work in tandem to generate strong particle clumping. The study by Xu & Bai (2022) was limited to a single  $St$  and a single magnetic field strength. In our study, we extend their work by performing simulations with multiple values of  $St$  in the range 0.01–0.1, and two different magnetic field strengths producing MRI turbulence with Shakura–Sunyaev viscosity parameters  $\alpha_{\text{SS}} = 10^{-4}$  and  $10^{-3}$ . For each combination of  $St$  and magnetic field strength, we perform simulations with varying dust-to-gas surface density ratios  $Z$ , in order to determine the clumping boundary. This constitutes the first parameter study of the SI interacting with nonideal MHD turbulence.

The paper is organized as follows. In Section 2, we briefly outline the methodology. Section 3 presents our results for  $Z_{\text{crit}}$ , comparisons with the clumping boundaries from L25 and L24, and the role of zonal flows. In Section 4, we discuss other types of turbulence and the limitations of the model. Finally, Section 5 summarizes the main conclusions.

## 2. Method

We use the local shearing-box approximation (Goldreich & Lynden-Bell 1965) to simulate the evolution of gas and particles in a small portion of a protoplanetary disk. Our 3D simulations include ambipolar diffusion and particle backreaction on the gas. Our methodology largely follows that of Xu & Bai (2022), with only minor modifications to the simulation setup. In the following, we provide a brief description of our model; for further details, we refer the reader to Xu & Bai (2022).

### 2.1. Numerical method

We consider an isothermal, non-self-gravitating, protoplanetary disk. We use the Athena MHD code (Stone et al. 2008) to model a small portion of the disk located at an arbitrary orbital radius and corotating with the Keplerian angular frequency  $\Omega_K$ . We ignore vertical gravity in the gas, i.e., the gas is unstratified, and thus the initial gas density  $\rho_0$  is uniform. We set the following code units:  $c_s = \Omega_K = \rho_0 = 1$ , where  $c_s$  is the isothermal sound speed. Given our choice of  $c_s$  and  $\Omega_K$ , the gas scale height would be  $H_g = 1$ . We apply shearing-periodic boundary conditions in the radial ( $x$ ) direction, and periodic boundary conditions in the azimuthal ( $y$ ) and vertical ( $z$ ) directions.

We impose a net vertical magnetic field  $B_0$ , the strength of which is characterized by the plasma  $\beta$ ,

$$\beta_0 \equiv \frac{\rho_0 c_s^2}{B_0^2 / 2\mu_0}, \quad (4)$$

which corresponds to the ratio of gas pressure to the magnetic pressure of the net vertical field. In the above equation,  $\mu_0$  is the permeability of vacuum, and we adopt the code units  $\mu_0 = 1$ . The strength of nonideal MHD effects is quantified by the Elsässer number, which for AD is given by

$$\text{Am} = \frac{\gamma \rho_i}{\Omega_K}, \quad (5)$$

where  $\gamma$  is the coefficient of momentum exchange in collisions between ions and neutrals, and  $\rho_i$  is the ion density. The limit  $\text{Am} \rightarrow \infty$  corresponds to ideal MHD, where the magnetic field is perfectly coupled to the gas.

Dust is modeled as Lagrangian particles and coupled to the gas via aerodynamic drag (Bai & Stone 2010b). The degree of aerodynamic coupling between gas and particles is characterized by  $\text{St}$ . We note that dust can also be modeled as a pressureless fluid; however, fluid-based models have been shown to reach lower peak dust densities for the SI than particle-based simulations (Baronett et al. 2026). The difference decreases with increasing resolution but is not completely eliminated even at  $1024^2$  resolution in axisymmetric, unstratified SI simulations. Since the computational cost of 3D SI simulations with non-ideal MHD at such high resolution is prohibitive for a parameter study, we adopt particle-based models that can be run at lower resolutions. Unlike particles, gas in protoplanetary disks is pressure-supported and orbits at a sub-Keplerian velocity, causing the particles to experience a headwind and drift radially toward the star. Rather than implementing the effects of the radial pressure gradient directly on the gas, a force is added to the particle equations of motion to mimic the outwardly decreasing radial pressure gradient of the gas. The pressure gradient is characterized by  $\Pi \equiv \eta v_K / c_s$ , where  $\eta v_K$  is the deviation from the Keplerian velocity  $v_K$ . We include vertical gravity (stratification) for the particles, allowing them to settle toward the midplane.

## 2.2. Simulation setup

Our shearing box is mapped onto a fixed, regular grid with a size of  $(0.8 \times 0.8 \times 0.8)H_g$ . The resolution is fixed at 250 cells per gas scale height. We adopt the same radial pressure gradient as in L24 and L25,  $\Pi = 0.05$ . Throughout this study, the Elsässer number is set to  $\text{Am} = 2$ , following Xu & Bai (2022), and two magnetic field strengths are considered,  $\beta_0 = 6 \times 10^4$  and  $\beta_0 = 6 \times 10^3$ . The corresponding wavelengths of fastest MRI growth are  $0.039H_g$  and  $0.122H_g$ , which gives a minimum resolution of 10 cells per wavelength. Particles in our simulations have fixed Stokes numbers. We explore  $\text{St} = 0.01, 0.03, \text{ and } 0.1$ .

Our aim is to identify the conditions under which the SI leads to strong clumping in a disk with self-consistently driven MRI turbulence. We adopt the same strong clumping criterion as Li & Youdin (2021), L24, and L25:

$$\rho_{p,\text{max}} > \rho_H = 9\rho_0 \sqrt{\frac{\pi}{8}} Q \approx 180\rho_0, \quad (6)$$

where  $\rho_{p,\text{max}}$  is the maximum particle density,  $\rho_H$  is the Hill density, and  $Q$  is the Toomre parameter (Toomre 1964). The Toomre parameter is set to  $Q = 32$  (implicitly defining a gravitational

constant  $G$ , though we do not actually compute gravity), consistent with previous work; this choice corresponds to a low-mass disk and yields a conservative threshold for strong clumping.

We perform simulations with varying dust-to-gas surface density ratios  $Z$  in order to determine  $Z_{\text{crit}}$  for each combination of  $\beta_0$  and  $\text{St}$ . Each simulation is initialized without particles and evolved for  $\sim 30$  orbital periods to allow the MRI to develop and fully saturate into turbulence. Particles are then inserted with random radial and azimuthal positions and a Gaussian vertical distribution with a particle scale height  $H_p$ , which is varied between simulations. The initial particle velocities follow the Nakagawa et al. (1986) equilibrium solution. We use  $200^3$  particles per simulation, corresponding to an average of one particle per grid cell. After insertion, particles settle toward the midplane. Simulations are evolved for just under 500 orbital periods, or until the Hill density is clearly exceeded, except in a few cases where they are extended to probe the late-time evolution.

## 3. Results

Figure 1 shows snapshots of the azimuthally averaged particle density for all simulations in the parameter study. For each simulation, we display the snapshot with the highest particle density among all saved outputs. The high-density clumps visible in many snapshots arise from a combination of particle trapping in zonal flows and concentration due to dust back-reaction (see Section 3.3). Runs with higher dust-to-gas surface density  $Z$  typically produce denser clumps. We note that the clumps seen in the  $x$ - $z$  plane are in fact high-density filaments that often extend across the entire  $y$ -extent of the simulation domain. The impact of MRI turbulence is evident in the diffusive part of the dust layer, which is far from regular. Simulations with smaller  $\text{St}$  have larger dust scale heights and exhibit larger, more diffuse clumps.

Simulations with lower plasma  $\beta$  exhibit stronger turbulence, leading to larger dust scale heights and less smooth dust layers. The strength of turbulence can be characterized in several ways, with one commonly used measure being the Shakura–Sunyaev stress parameter ( $\alpha_{\text{SS}}$ ; Shakura & Sunyaev 1973). The parameter  $\alpha_{\text{SS}}$  quantifies the rate of angular momentum transport in the disk and is defined as

$$\alpha_{\text{SS}} \equiv \frac{-\langle B_x B_y \rangle / \mu_0 + \langle \rho_0 u_x u_y \rangle}{\rho_0 c_s^2}, \quad (7)$$

where  $B$  is the magnetic field strength and  $u$  is the gas velocity. The first term represents the Maxwell stress, while the second corresponds to the Reynolds stress; the total stress is normalized by the thermal pressure. We measure  $\alpha_{\text{SS}}$  in simulations without dust feedback and obtain approximately  $\alpha_{\text{SS}} \approx 10^{-4}$  and  $\alpha_{\text{SS}} \approx 10^{-3}$  for  $\beta_0 = 6 \times 10^4$  and  $\beta_0 = 6 \times 10^3$ , respectively (see Table 2).

### 3.1. Threshold for strong clumping

Figure 2 shows the time evolution of the maximum particle density for all simulations in the parameter study. Simulations in which the maximum density exceeds the Hill density (dotted line; Eq. 6) are classified as exhibiting strong clumping and are shown in Figure 3 as solid circles. We emphasize that strong clumping is not necessarily synonymous with SI clumping, which is typically identified by the presence of distinct clumps in the  $z$ - $x$  plane and a sharp increase in maximum particle density. For example, the simulation with  $\beta_0 = 6 \times 10^4$ ,  $\text{St} = 0.01$ , and  $Z = 0.02$  shows clear signatures of SI clumping, but does not satisfy our criterion for strong clumping.

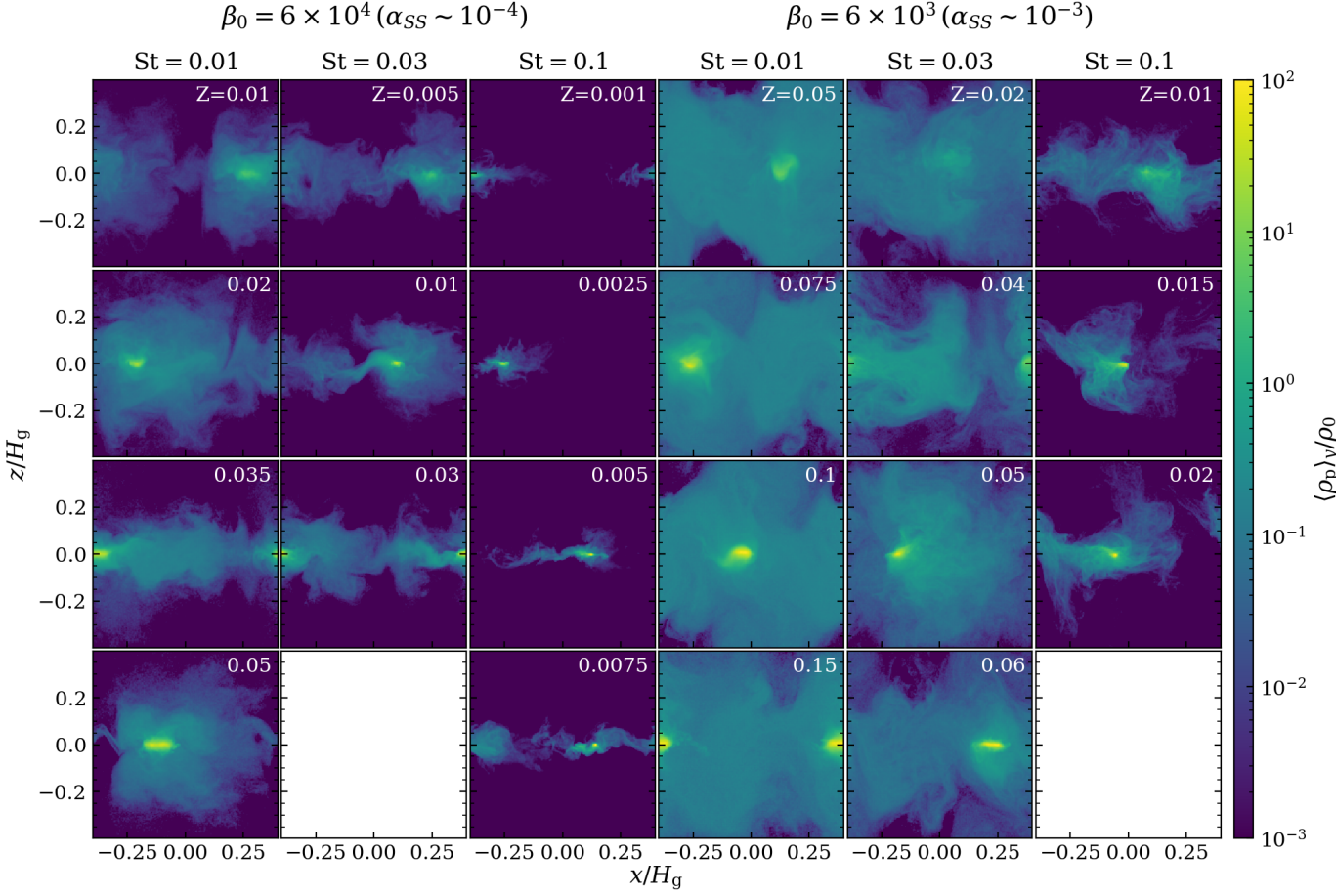


Fig. 1: Snapshots of the azimuthally averaged particle density for all simulations in the parameter study. For each simulation, we show the snapshot with the highest particle density among all saved outputs. The three leftmost columns correspond to simulations with  $\beta_0 = 6 \times 10^4$ , yielding  $\alpha_{SS} \sim 10^{-4}$ , while the three rightmost columns correspond to simulations with  $\beta_0 = 6 \times 10^3$ , yielding  $\alpha_{SS} \sim 10^{-3}$ . The dust-to-gas surface density ratio ( $Z$ ) of each simulation is indicated in the top-right corner of each panel.

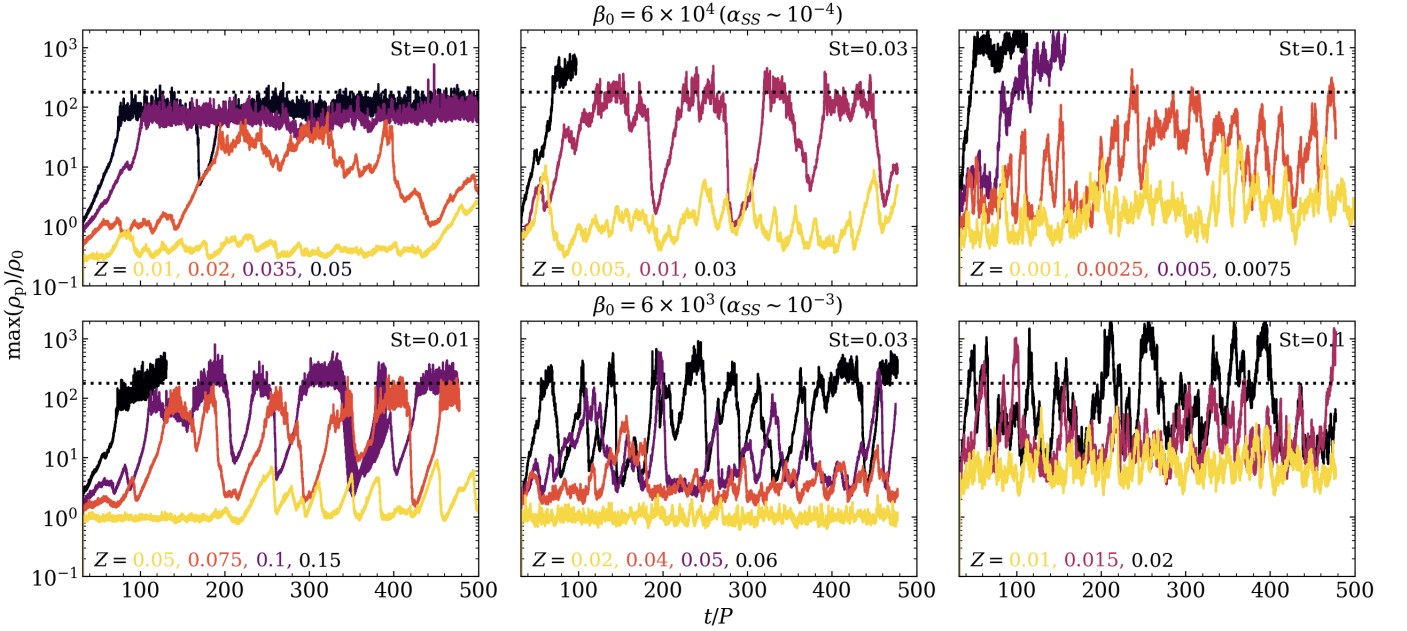


Fig. 2: Maximum particle density as a function of time scaled by orbital period  $P$  for all simulations in the parameter study. The dotted line indicates the Hill density (Eq. (6)), and the dust-to-gas surface density ratio  $Z$  for each simulation is shown in the bottom-left corner of each panel.

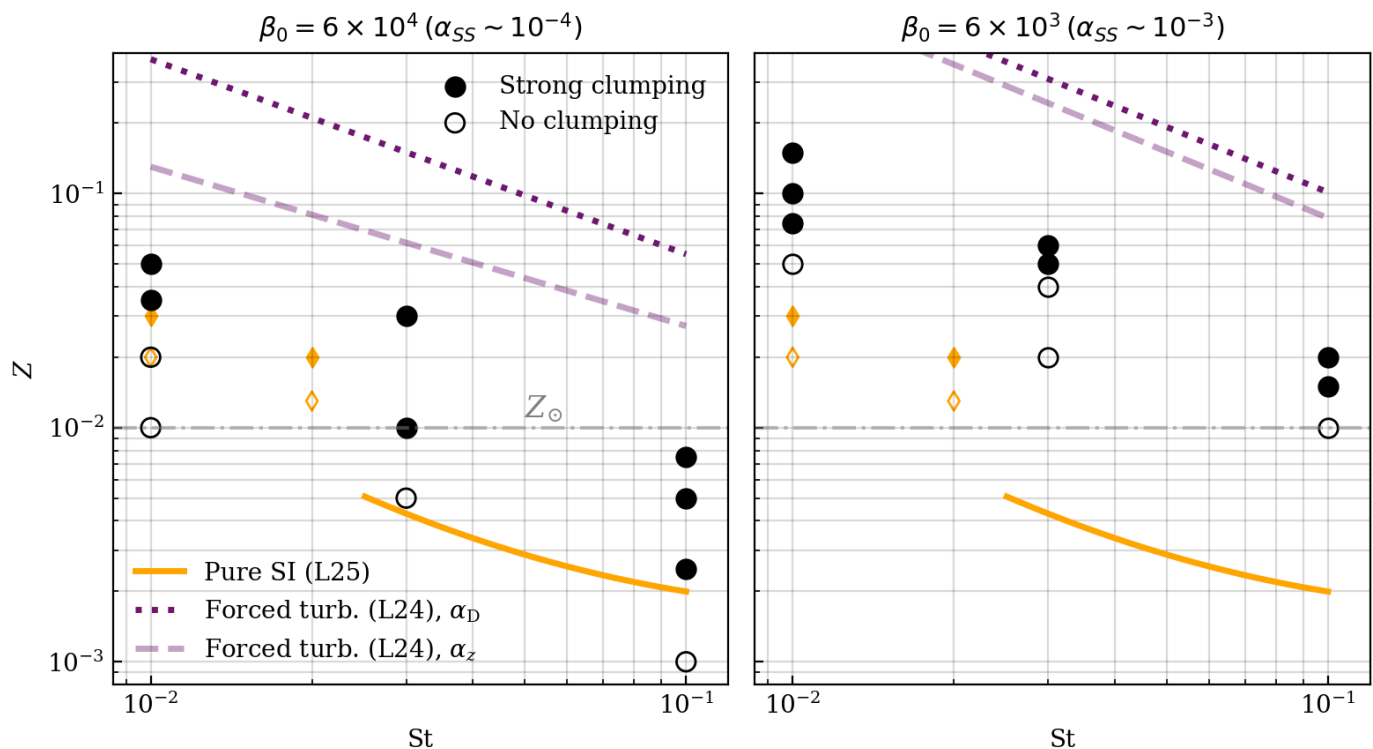


Fig. 3: Overview of all simulations in the parameter study, showing whether they exhibit strong clumping (filled circles) or not (empty circles). Results from the 3D pure SI simulations by L25 are shown as a solid orange line and diamond markers, where filled markers indicate strong clumping. The dashed and dotted purple lines show the comparison with L24, who performed 3D SI simulations including isotropically forced turbulence. Our simulations with relatively weak turbulence (left panel) show  $Z_{\text{crit}}$  similar to the non-turbulent cases, whereas stronger turbulence (right panel) results in higher  $Z_{\text{crit}}$ , although still significantly smaller than in the isotropically forced-turbulence models.

Since we do not model particle self-gravity, no actual planetesimals form in the simulations, and the dense clumps and filaments that develop are often transient. As in previous parameter studies,  $Z_{\text{crit}}$  decreases with increasing  $St$ , at least over the range of  $St$  considered here. In simulations with relatively weak turbulence  $\alpha_{SS} \sim 10^{-4}$ , strong clumping is observed for dust-to-gas ratios as low as  $Z = 0.25Z_{\odot}$ , where  $Z_{\odot} = 0.01$  is the solar dust-to-gas ratio. For  $St < 0.03$ , supersolar dust-to-gas ratios are required. In simulations with stronger turbulence  $\alpha_{SS} \sim 10^{-3}$ , supersolar dust-to-gas ratios are required regardless of  $St$ . In this regime, particle concentration by dust back-reaction and MRI zonal flows is insufficient for planetesimal formation to occur with a Solar dust-to-gas ratio and particles with a single, fixed Stokes number. A proper treatment of dust growth could change this, as recent studies have shown that dust clumping by the SI and dust growth boost each other (Ho et al. 2024; Carrera et al. 2025; Tominaga & Tanaka 2025; Vallucci-Goy et al. 2026; Pierens et al. 2026).

Some previous parameter studies, including L24 and L25, also present the clumping boundary in terms of the midplane dust-to-gas volume density ratio  $\epsilon$ . Unlike  $Z$ , which is a simulation input parameter,  $\epsilon$  must be measured from the simulations. To obtain a reliable value of  $\epsilon$ , it is typically measured during the pre-clumping phase, defined as the interval after an equilibrium dust layer has formed but before significant clumps or filaments appear; this is also the phase during which the particle scale height is measured. In our study, a significant fraction of the simulations do not exhibit a well-defined pre-clumping phase. As a result, we are unable to apply the same procedure to

obtain a reliable estimate of  $\epsilon$  or  $H_p$ . Therefore, we choose not to present the clumping boundary in terms of  $\epsilon$ .

### 3.2. Comparison with pure SI and isotropically forced-turbulence studies

The solid orange line and diamond markers in Fig. 3 show the results of the pure SI simulations in 3D from L25 (Eq. 2). Our  $Z_{\text{crit}}$  agrees well with the results of L25 in the case of relatively weak MRI turbulence. This suggests that MRI-driven turbulence with AD does not hinder planetesimal formation, provided that the turbulence is not too strong. When the turbulence strength is increased by a factor of ten (right panel of Fig. 3),  $Z_{\text{crit}}$  becomes several times higher than in the weak-turbulence scenario. Strong MRI turbulence thus weakens particle concentration.

We note that our comparison with L25 is not a one-to-one comparison, since the simulation setups are quite different. The lack of external turbulence in L25 allows them to adopt a smaller vertical box height, and they use a fiducial domain size of  $(0.8 \times 0.2 \times 0.2)H_g$ , whereas we adopt  $(0.8 \times 0.8 \times 0.8)H_g$ . They also use a higher fiducial resolution of  $640H_g^{-1}$ , compared to our resolution of  $250H_g^{-1}$ . The lower resolution in our study is due to the increased computational cost associated with the larger domain size and the inclusion of MHD. Finally, L25 adopts outflow boundary conditions in the vertical direction. In SI simulations, particle–gas interactions near the midplane can drive gas perturbations away from the midplane, which may reflect and induce additional particle stirring when periodic or reflecting boundary

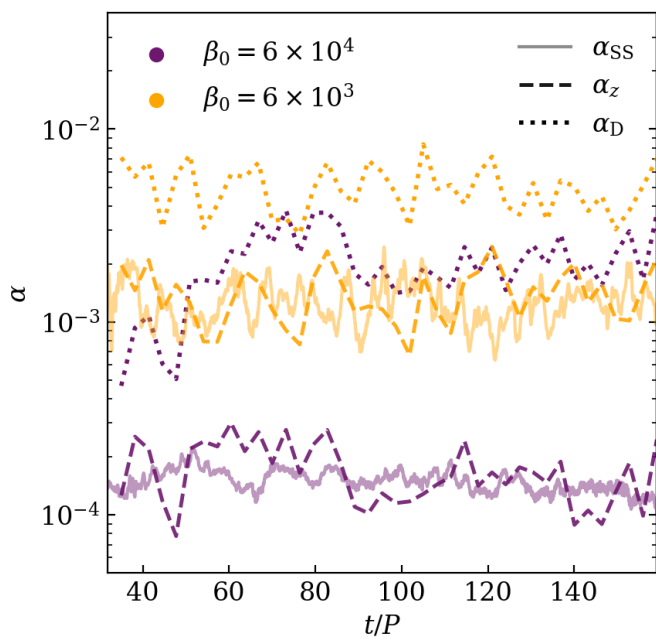


Fig. 4: Time evolution of the three turbulent parameters  $\alpha_{SS}$  (Eq. (7)),  $\alpha_z$  (Eq. (8)), and  $\alpha_D$  (Eq. (9)), measured in simulations without particle feedback and with  $St = 0.1$ .

conditions are used (Li et al. 2018). In our work, we assume that turbulence generated by the MRI dominates over any additional stirring introduced by the vertical boundary conditions.

To compare with the SI simulations of L24 that include isotropically forced turbulence, we first need to calculate the turbulence parameters  $\alpha_D$  and  $\alpha_z$  used in that study. To this end, we perform simulations without particle feedback and with  $St = 0.1$ . The parameter  $\alpha_z$  represents gaseous diffusion in the vertical direction and is obtained by assuming a balance between vertical settling and turbulent diffusion of the dust particles driven by the gas turbulence:

$$\alpha_z = St \left[ \frac{(H_p/H_g)^2}{1 - (H_p/H_g)^2} \right]. \quad (8)$$

We estimate the particle scale height  $H_p$  by fitting a Gaussian to the radially and azimuthally averaged particle density. The time evolution of  $\alpha_z$  is shown as dashed lines in Fig. 4, and the time averages of  $H_p$  and  $\alpha_z$  are provided in Table 2. Our calculations of  $\alpha_z$  and  $\alpha_{SS}$  are in close agreement, suggesting that  $\alpha_{SS}$  is a good measure of the dust layer thickness in these simulations.

The parameter  $\alpha_D$ , which represents the total spatial diffusion of turbulent gas, can be related to  $\alpha_z$  via

$$\alpha_D = \alpha_z(l^2 + m^2 + 1), \quad (9)$$

where  $l \equiv \delta u'_x / \delta u'_z$  and  $m \equiv \delta u'_y / \delta u'_z$  (see derivation in L24, eq. 13-15). The velocity fluctuations of the  $i$ th component are calculated as

$$\delta u'_i \equiv \sqrt{\langle u_i'^2 \rangle - \langle u_i' \rangle^2}, \quad (10)$$

where  $u'_i$  represents the gas velocity after subtraction of the Keplerian shear. The time evolution of  $\alpha_D$  is shown in Fig. 4 as dotted lines, and the time-averaged values of  $\alpha_D$  and the components of  $\delta u'$  are provided in Table 2.

In the case of isotropic turbulence,  $\alpha_D = 3\alpha_z$ . The MRI turbulence in our strong-field simulation with  $\beta_0 = 6 \times 10^3$  is close to isotropic, with  $\alpha_D \approx 3.5\alpha_z$ . In contrast, the MRI turbulence in the weak-field simulation with  $\beta_0 = 6 \times 10^4$  is highly anisotropic, with  $\alpha_D \gg 3\alpha_z$ . A comparison of the components of the velocity fluctuations reveals that the azimuthal velocity fluctuations are significantly stronger than those in the radial and vertical directions. The increase of  $\alpha_D$  until  $t \sim 70P$  is consistent with the emergence of a strong zonal flow, which reaches its maximum width around that time and persists until the end of the simulation.

We use the time-averaged values of  $\alpha_z$  and  $\alpha_D$  in the fit of L24 (Eq. 3) and obtain the dashed and dotted lines in Fig. 3. Regardless of which of the two turbulence measures is used in the comparison, we obtain significantly lower  $Z_{crit}$  for strong clumping in our study, indicating that self-consistently generated MRI turbulence poses a smaller obstacle to planetesimal formation than forced turbulence. The reason is that the MRI generates zonal flows, which aid in particle concentration, whereas forced turbulence acts only to diffuse particles. In the case of relatively weak turbulence, the concentrating effect counteracts diffusion, leading to values of  $Z_{crit}$  comparable to those obtained in pure SI simulations. As the turbulence strength is increased, however, diffusion becomes dominant and  $Z_{crit}$  increases. This is in agreement with the findings of L24, which find that SI clumping is prevented when turbulence only acts to diffuse dust.

Similar to our comparison with L25, our comparison with L24 is not a one-to-one comparison. They use a domain of size  $L_x = 0.4H_g$ ,  $L_y = 0.2H_g$ , and  $L_z$  between  $0.8 - 2H_g$ , with larger  $L_z$  used in runs with high turbulence and/or small Stokes numbers. They also use a higher resolution of  $640H_g^{-1}$ . Finally, the simulations of L25 include particle self-gravity, and their clumping criterion is based on gravitational collapse. This is a stricter clumping criterion than exceeding the Hill density, because after reaching the Hill density the dust clump also needs to overcome diffusion at smaller scales in order for collapse to occur.

### 3.3. The role of zonal flows

Zonal flows are large-scale azimuthal structures that produce density and pressure variations in the saturated MRI (Johansen et al. 2009; Bai & Stone 2014). Local pressure variations within them translate into changes in the radial drift of particles, and zero pressure gradients in pressure maxima result in particle trapping (Whipple 1972). The role of zonal flows in clumping is best assessed by comparing the locations of particle clumps with the locations of the zonal flows. At a pressure maximum, the gas orbits at the Keplerian velocity, so  $u'_y = 0$ , and the gas density reaches a local maximum. Positive pressure gradients correspond to  $u'_y > 0$ , while negative pressure gradients correspond to  $u'_y < 0$ . When identifying zonal flows from the gas density profile, one must keep in mind that in our model, a background pressure gradient is implemented via a radial force; consequently, any pressure maximum appears on the left, negative- $x$  side of the corresponding gas density maximum.

Figure 5 shows the time evolution of the azimuthally averaged particle density, gas density, and gas azimuthal velocity in the midplane for two simulations that exhibit strong clumping. Since the radial pressure gradient is added to the particles instead of the gas, we subtracted  $\Pi$  from  $u'_y$  in this figure. Consistent with Xu & Bai (2022), we find a clear correspondence between the locations of particle clumps and zonal flows. In the top panels, which show data from the simulation with  $\beta_0 = 6 \times 10^4$ ,  $St = 0.03$ , and  $Z = 0.01$ , a particle filament de-

$\beta_0$	$H_p$	$\alpha_z$	$\delta u'_x$	$\delta u'_y$	$\delta u'_z$	$\alpha_D$	$-B_x B_y$	$\rho_0 u_x u_y$	$\alpha_{SS}$
$6 \times 10^4$	0.04086	0.00017	0.01326	0.03701	0.01208	0.00201	0.00012	0.00003	0.00015
$6 \times 10^3$	0.11678	0.00140	0.03879	0.04201	0.03595	0.00498	0.00095	0.00032	0.00127

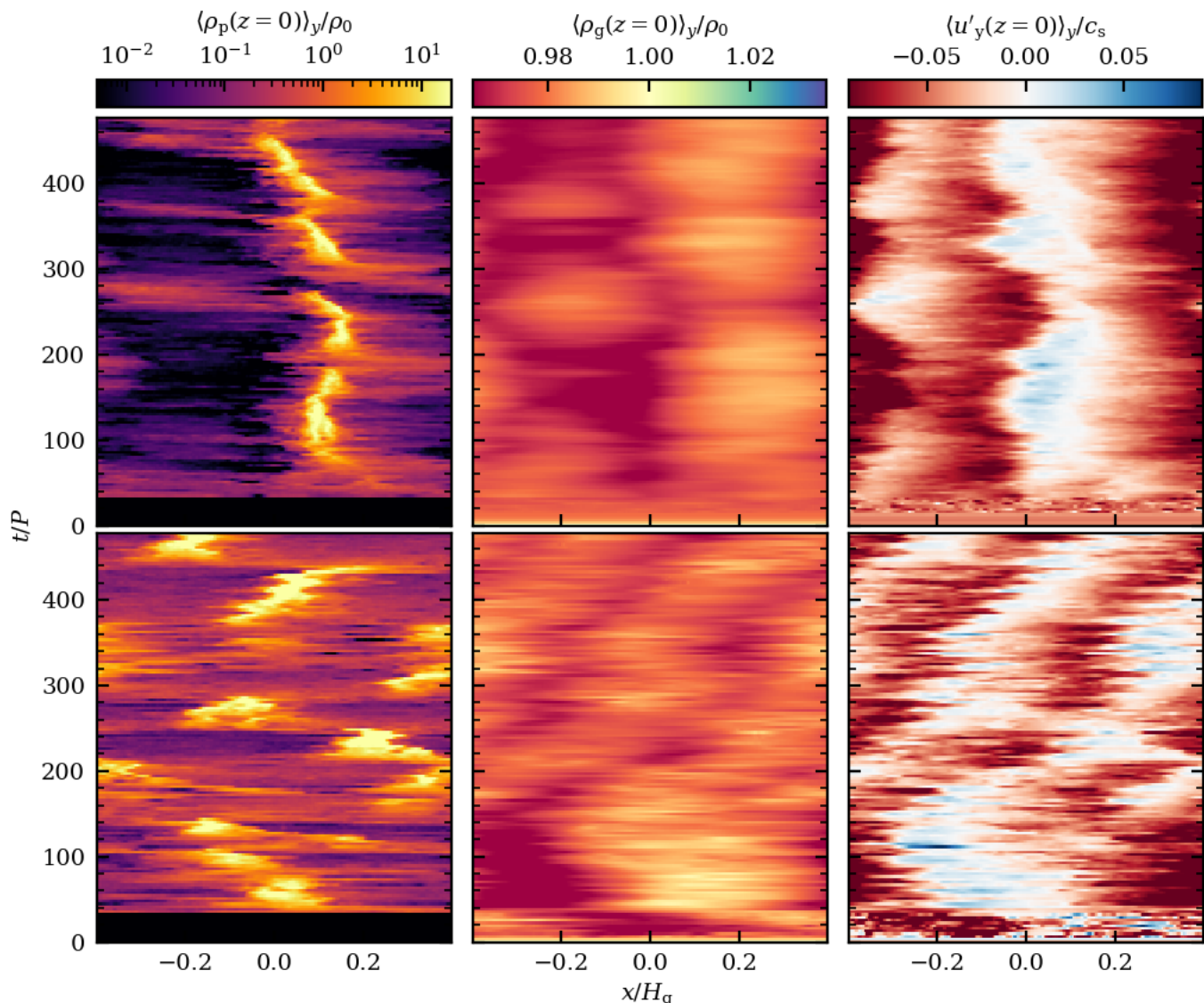
Table 2: Time-averaged quantities measured from simulations performed without particle feedback and using  $St = 0.1$ .

Fig. 5: Time evolution of the azimuthally averaged particle density (*left*), gas density (*middle*), and gas azimuthal velocity corrected for the background pressure gradient (*right*) at the midplane (vertically averaged  $\pm 1$  cell from  $z = 0$ ), for the strong-clumping runs with  $\beta_0 = 6 \times 10^4$ ,  $St = 0.03$ ,  $Z = 0.01$  (*top*) and  $\beta_0 = 6 \times 10^3$ ,  $St = 0.03$ ,  $Z = 0.06$  (*bottom*). Particles preferentially concentrate in zonal flows, identifiable as regions where the corrected  $u'_y = 0$  in the right column.

velops at  $x/H_g \simeq 0.1$  after approximately 80 orbital periods. The filament subsequently disappears and re-emerges several times, but remains at roughly the same radial location. This location lies to the left of the gas density maximum and coincides with regions where  $u'_y \sim 0$ , as expected.

In our simulation with  $\beta_0 = 6 \times 10^3$ ,  $St = 0.03$ , and  $Z = 0.06$  (bottom panels of Fig. 5), we likewise find a strong correspondence between the locations of particle filaments and zonal flows. In this case, the zonal flows - and consequently the particle filaments - are more transient and appear at different

radial locations over time. We note that the presence of zonal flows does not, by itself, guarantee strong clumping, as our non-clumping runs also exhibit zonal flows.

It should be noted that at exactly  $\Pi = 0$  there is no radial drift, and the SI is therefore formally absent. However, the pressure bumps associated with zonal flows are dynamically active, so the zero gradient region fluctuates in position, as can be seen in Fig. 5. As a result, the SI can grow across the pressure bump. Studies of SI in idealized pressure bumps by Carrera et al. (2021) showed the growth of SI in the finite gradient regions, producing

the fluctuations necessary to allow growth throughout the structure. Xu & Bai (2022) further demonstrated reduced maximum particle densities in zonal flows when SI was prevented by turning off dust drag on the gas.

## 4. Discussion

### 4.1. Other types of turbulence

Turbulence in protoplanetary disks can be generated by multiple (magneto)hydrodynamical processes, with different mechanisms dominating in different regions of the disk (Lesur et al. 2023). Several turbulence-driving processes may also coexist, such as the MRI and the VSI (Cui & Bai 2022). As demonstrated by the comparison between our simulations and those of L24, the forcing-scale properties of the turbulence play a crucial role in particle clumping. In other words, two different turbulence-driving mechanisms that produce the same overall turbulence strength as characterized by various turbulent parameters do not necessarily yield the same clumping threshold. This is because self-consistently driven turbulence not only introduces diffusive effects, but can also modify the disk structure, for example through the formation of pressure bumps or anti-cyclonic vortices. Both diffusion and disk structure strongly influence particle dynamics, and therefore the ability of the SI to concentrate particles.

The study by L24, which employs forced isotropic turbulence, represents the least favorable scenario for particle clumping by the SI, since the turbulence is purely diffusive and does not generate pressure variations or anisotropies that can aid particle concentration. In contrast, in our nonideal MHD simulations including AD, clumping arises from a combination of concentration due to dust back-reaction and particle trapping within zonal flows. Such zonal flows have been reported in both local (Riols & Lesur 2018) and global (Cui & Bai 2021) simulations of nonideal MHD with AD, as well as in simulations with ideal MHD (Johansen et al. 2009; Bai & Stone 2014). Turbulence is significantly stronger in the ideal MHD regime, and although planetesimal formation via the SI is indeed possible under these conditions (Johansen et al. 2007, 2011), such environments are expected to be found only in the innermost regions of protoplanetary disks (Armitage 2011).

Turning to purely hydrodynamical processes, one mechanism that has received considerable attention in recent years is the VSI. The VSI has been shown to coexist with both the SI (Schäfer & Johansen 2022) and the MRI (Cui & Bai 2022). Global simulations including both the SI and the VSI find that the VSI can trigger the Rossby wave instability, leading to the formation of vortices that work in concert with the SI to concentrate particles and form planetesimals (Huang & Bai 2025a,b).

### 4.2. Limitations of the model

Both the MRI and SI are sensitive to numerical parameters such as domain size and spatial resolution (Yang et al. 2009, 2012; Yang & Johansen 2014; Li et al. 2018). The wavelength of the fastest MRI growth is resolved by at least ten cells in our models, and we fit a minimum of six wavelengths into the vertical extent of the simulation domain (Sano et al. 2004). Modifying the resolution or box height affects the properties of the MRI turbulence, such as the values of the various turbulent parameters. We find that an increase in resolution and box size both lead to an increase in  $\alpha_{SS}$ . Xu & Bai (2022) also report weaker zonal flows in runs with higher resolution. Furthermore, while zonal flows

have been shown to be a natural outcome of MRI turbulence in both local simulations and global disk settings, the properties of the zonal flows may still be sensitive to the simulation setup.

The particle scale heights in our parameter study vary between  $\sim 0.03H_g$  and  $\sim 0.2H_g$ , as estimated from simulations with a clear pre-clumping phase, resulting in a minimum grid resolution of  $\sim 8H_p^{-1}$ . We adopt a particle resolution of one particle per grid cell, as done in several previous studies. Although an increased particle resolution would result in reduced Poisson noise, the number of particles per grid cell does not strongly affect clumping by the SI (Bai & Stone 2010b). Since the clumping boundary is sensitive to numerical details, additional simulations with larger domain sizes and higher grid and particle resolution would be required to further solidify our findings. As mentioned above, such modifications also affect the turbulence properties, which in turn influence the clumping threshold. Given these complications and the large computational cost associated with such explorations, we do not pursue a detailed convergence study here, but leave this for future work.

Our study, which constitutes the first parameter study of the SI in the presence of self-consistently generated MRI turbulence, is limited to two magnetic field strengths and three Stokes numbers. Deriving a fit to the clumping boundary, analogous to those presented in L24 and L25, would require additional simulations, which we leave for future work. Furthermore, all simulations were performed with a constant global radial pressure gradient of  $\Pi = 0.05$ , consistent with previous studies of the SI clumping boundary. Since the pressure gradient can vary with disk radius – even in disks without local pressure variations – it would be desirable to derive a fit that explicitly accounts for its effect; this would require simulations spanning a range of pressure gradients.

Our strong clumping criterion is based on the Hill density, which varies with location and disk mass. For example, weaker clumping may still trigger collapse farther out in the disk even if it does not in the inner disk. The clumping boundary we obtain is therefore not universal and may shift depending on disk location and disk mass. Finally, this study assumes particles with a single  $St$ , whereas real disks contain a distribution of particle sizes. The polydisperse SI has been explored using both linear (Krapp et al. 2019; Paardekooper et al. 2021; Zhu & Yang 2021) and nonlinear (Bai & Stone 2010a; Schaffer et al. 2021; Yang & Zhu 2021) simulations, with mixed results. To date, a clumping boundary for the polydisperse SI remains to be established.

## 5. Conclusions

We present the first parameter study of the SI in 3D stratified simulations including self-consistently generated MRI turbulence. We model a local patch of the outer protoplanetary disk, where the dominant nonideal MHD effect is ambipolar diffusion. We perform simulations with two magnetic field strengths, three Stokes numbers  $St = 0.01, 0.03$  and  $0.1$ , and varying dust-to-gas surface density ratios  $Z$  in order to identify the boundary for strong clumping. Our main findings can be summarized as follows:

- In the case of modest turbulence with  $\alpha_{SS} \sim 10^{-4}$ , the clumping boundary remains close to that obtained from pure SI simulations. This demonstrates that turbulence does not necessarily hinder planetesimal formation. We find significantly subsolar  $Z_{crit}$  for  $St = 0.1$ , while supersolar  $Z_{crit}$  is required for  $St < 0.03$ . When the turbulence strength is increased to

$\alpha_{SS} \sim 10^{-3}$ ,  $Z_{crit}$  becomes supersolar for all considered values of  $St$ .

- A comparison with forced-turbulence models shows that our inferred  $Z_{crit}$  values are significantly lower, indicating that self-consistently generated turbulence that produces driving-scale structures can pose a smaller obstacle to planetesimal formation than isotropically forced turbulence that primarily acts to diffuse dust particles.
- Clumping in our simulations occurs within zonal flows – large-scale azimuthal density and pressure variations generated by MRI turbulence – that act to concentrate particles and, together with dust back-reaction, generate particle clumps.

*Acknowledgements.* We thank P. Armitage and D. Sengupta for useful discussions. LEJE and M-MML acknowledge support from NASA via the Emerging Worlds program under grant #80NSSC25K7117. ZX acknowledges support from the European Union's Horizon Europe research and innovation programme under the Marie Skłodowska-Curie grant agreement No. 101211616 (PLANDEVOL) and the Carlsberg Foundation (Semper Ardens: Advance grant FIRSTATMO). CCY acknowledges the support from NASA via the Emerging Worlds program (#80NSSC23K0653), the Astrophysics Theory Program (grant #80NSSC24K0133), and the Theoretical and Computational Astrophysical Networks (grant #80NSSC21K0497). PH acknowledges support from the National Science Foundation of China under grant Nos. 12503070, 12233004 and 12533011. J.L. acknowledges support from NASA under the Future Investigators in NASA Earth and Space Science and Technology grant #80NSSC22K1322.

## References

- Armitage, P. J. 2011, *ARA&A*, 49, 195
- Bai, X.-N. & Stone, J. M. 2010a, *ApJ*, 722, 1437
- Bai, X.-N. & Stone, J. M. 2010b, *ApJS*, 190, 297
- Bai, X.-N. & Stone, J. M. 2010c, *ApJ*, 722, L220
- Bai, X.-N. & Stone, J. M. 2011, *ApJ*, 736, 144
- Bai, X.-N. & Stone, J. M. 2014, *The Astrophysical Journal*, 796, 31
- Balbus, S. A. & Hawley, J. F. 1991, *ApJ*, 376, 214
- Barnes, J. T., Schwartz, S. R., & Jacobson, S. A. 2025, *ApJ*, 990, 130
- Barnes, J. T., Schwartz, S. R., & Jacobson, S. A. 2026, arXiv e-prints, arXiv:2602.16056
- Baronett, S. A., Lyra, W., Aly, H., et al. 2026, arXiv e-prints, arXiv:2603.04558
- Birnstiel, T., Klahr, H., & Ercolano, B. 2012, *A&A*, 539, A148
- Blum, J. & Wurm, G. 2008, *ARA&A*, 46, 21
- Carrera, D., Johansen, A., & Davies, M. B. 2015, *A&A*, 579, A43
- Carrera, D., Lim, J., Eriksson, L. E. J., Lyra, W., & Simon, J. B. 2025, *A&A*, 696, L23
- Carrera, D., Simon, J. B., Li, R., Kretke, K. A., & Klahr, H. 2021, *AJ*, 161, 96
- Chandrasekhar, S. 1960, *Proceedings of the National Academy of Science*, 46, 253
- Cui, C. & Bai, X.-N. 2021, *MNRAS*, 507, 1106
- Cui, C. & Bai, X.-N. 2022, *MNRAS*, 516, 4660
- Drążkowska, J., Bitsch, B., Lambrechts, M., et al. 2023, in *Astronomical Society of the Pacific Conference Series*, Vol. 534, *Protostars and Planets VII*, ed. S. Inutsuka, Y. Aikawa, T. Muto, K. Tomida, & M. Tamura, 717
- Goldreich, P. & Lynden-Bell, D. 1965, *MNRAS*, 130, 125
- Güttler, C., Blum, J., Zsom, A., Ormel, C. W., & Dullemond, C. P. 2010, *A&A*, 513, A56
- Ho, K. W., Li, H., & Li, S. 2024, *ApJ*, 975, L34
- Huang, P. & Bai, X.-N. 2025a, *ApJ*, 986, L13
- Huang, P. & Bai, X.-N. 2025b, *ApJ*, 986, 76
- Johansen, A., Klahr, H., & Henning, T. 2011, *A&A*, 529, A62
- Johansen, A., Mac Low, M.-M., Lacerda, P., & Bizzarro, M. 2015, *Science Advances*, 1, 1500109
- Johansen, A., Oishi, J. S., Mac Low, M.-M., et al. 2007, *Nature*, 448, 1022
- Johansen, A. & Youdin, A. 2007a, *ApJ*, 662, 627
- Johansen, A. & Youdin, A. 2007b, *ApJ*, 662, 627
- Johansen, A., Youdin, A., & Klahr, H. 2009, *ApJ*, 697, 1269
- Kavelaars, J. J., Petit, J.-M., Gladman, B., et al. 2021, *ApJ*, 920, L28
- Krapp, L., Benítez-Llambay, P., Gressel, O., & Pessah, M. E. 2019, *The Astrophysical Journal, Letters*, 878, L30
- Lesur, G., Flock, M., Ercolano, B., et al. 2023, in *Astronomical Society of the Pacific Conference Series*, Vol. 534, *Protostars and Planets VII*, ed. S. Inutsuka, Y. Aikawa, T. Muto, K. Tomida, & M. Tamura, 465
- Li, R. & Youdin, A. N. 2021, *ApJ*, 919, 107
- Li, R., Youdin, A. N., & Simon, J. B. 2018, *ApJ*, 862, 14
- Lim, J., Simon, J. B., Li, R., et al. 2024, *ApJ*, 969, 130
- Lim, J., Simon, J. B., Li, R., et al. 2025a, arXiv e-prints, arXiv:2509.18270
- Lim, J., Simon, J. B., Li, R., et al. 2025b, *ApJ*, 981, 160
- Nakagawa, Y., Sekiya, M., & Hayashi, C. 1986, *Icarus*, 67, 375
- Nelson, R. P., Gressel, O., & Umurhan, O. M. 2013, *MNRAS*, 435, 2610
- Nesvorný, D., Li, R., Youdin, A. N., Simon, J. B., & Grundy, W. M. 2019, *Nature Astronomy*, 3, 808
- Paardekooper, S.-J., McNally, C. P., & Lovascio, F. 2021, *Monthly Notices of the Royal Astronomical Society*, 502, 1579
- Pierens, A., Collin-Dufresne, T., Lin, M.-K., & DiFolco, E. 2026, *A&A*, 706, A67
- Pinte, C., Teague, R., Flaherty, K., et al. 2023, in *Astronomical Society of the Pacific Conference Series*, Vol. 534, *Protostars and Planets VII*, ed. S. Inutsuka, Y. Aikawa, T. Muto, K. Tomida, & M. Tamura, 645
- Riols, A. & Lesur, G. 2018, *A&A*, 617, A117
- Sano, T., Inutsuka, S.-i., Turner, N. J., & Stone, J. M. 2004, *ApJ*, 605, 321
- Schäfer, U. & Johansen, A. 2022, *A&A*, 666, A98
- Schäfer, U., Johansen, A., & Flock, M. 2025, *A&A*, 694, A57
- Schaffer, N., Johansen, A., & Lambrechts, M. 2021, *A&A*, 653, A14
- Sekiya, M. & Onishi, I. K. 2018, *ApJ*, 860, 140
- Shakura, N. I. & Sunyaev, R. A. 1973, *A&A*, 500, 33
- Simon, J. B., Armitage, P. J., Li, R., & Youdin, A. N. 2016, *ApJ*, 822, 55
- Stone, J. M., Gardiner, T. A., Teuben, P., Hawley, J. F., & Simon, J. B. 2008, *ApJS*, 178, 137
- Tominaga, R. T. & Tanaka, H. 2025, *ApJ*, 983, 15
- Toomre, A. 1964, *ApJ*, 139, 1217
- Vallucci-Goy, V., Lebreuilly, U., Mac Low, M.-M., & Hennebelle, P. 2026, *A&A*, 705, L1
- Velikhov, E. P. 1959, *Soviet Journal of Experimental and Theoretical Physics*, 9, 995
- Villenave, M., Stapelfeldt, K. R., Duchêne, G., et al. 2022, *ApJ*, 930, 11
- Weidenschilling, S. J. 1977, *MNRAS*, 180, 57
- Whipple, F. L. 1972, in *From Plasma to Planet*, ed. A. Elvius, 211
- Xu, Z. & Bai, X.-N. 2022, *ApJ*, 924, 3
- Yang, C.-C. & Johansen, A. 2014, *ApJ*, 792, 86
- Yang, C.-C., Johansen, A., & Carrera, D. 2017, *A&A*, 606, A80
- Yang, C.-C., Mac Low, M.-M., & Johansen, A. 2018, *ApJ*, 868, 27
- Yang, C.-C., Mac Low, M.-M., & Menou, K. 2009, *ApJ*, 707, 1233
- Yang, C.-C., Mac Low, M.-M., & Menou, K. 2012, *ApJ*, 748, 79
- Yang, C. C. & Zhu, Z. 2021, *Monthly Notices of the Royal Astronomical Society*, 508, 5538
- Youdin, A. N. & Goodman, J. 2005, *ApJ*, 620, 459
- Zhu, Z. & Yang, C. C. 2021, *Monthly Notices of the Royal Astronomical Society*, 501, 467